Unique Dirac and triple point fermiology in simple transition metals and their binary alloys

Chiranjit Mondal,[1,*] Chanchal K. Barman,[2,*] Shuvam Sarkar,[3] Sudipta Roy Barman,[3] Aftab Alam,[2,†] and Biswarup Pathak[1,4,‡]

[1]*Discipline of Metallurgy Engineering and Materials Science, IIT Indore, Simrol, Indore 453552, India*
[2]*Department of Physics, Indian Institute of Technology, Bombay, Powai, Mumbai 400076, India*
[3]*UGC-DAE Consortium for Scientific Research, Khandwa Road, Indore 452001, Madhya Pradesh, India*
[4]*Discipline of Chemistry, School of Basic Sciences, IIT Indore, Simrol, Indore 453552, India*

(Received 17 September 2019; revised manuscript received 15 March 2020; accepted 17 March 2020; published 7 April 2020)

Noble-metal surfaces (Au, Ag, Cu, etc.) have been extensively studied for Shockley-type surface states (SSs). Very recently, some of these Shockley SSs have been understood from the topological consideration, with the knowledge of global properties of electronic structure. In this paper, we show the existence of Dirac-like excitations in the elemental noble-metal Ru, Re, and Os based on symmetry analysis and *first-principles calculations*. The unique SS-driven Fermi arcs have been investigated in detail for these metals. Our calculated SSs and Fermi arcs are consistent with the previous transport and photoemission results. We attribute this Dirac excitation-mediated Fermi arc topology as the possible reason for several existing transport anomalies, such as large nonsaturating magnetoresistance, the anomalous Nernst electromotive force and its giant oscillations, magnetic breakdown, etc. We further show that the Dirac-like excitations in these elemental metals can further be tuned to three component Fermionic excitations, using a symmetry-allowed alloy mechanism.

DOI: 10.1103/PhysRevB.101.155108

I. INTRODUCTION

Symmetry-protected multifold band crossings in momentum space often exhibit a strong topological response in the transport measurement. A fourfold Dirac node [1] splits into a pair of twofold Weyl nodes [2] under magnetic field, which in turn shows several anomalous transport signatures, such as the anomalous Hall effect [3–6], the anomalous Nernst effect [7–9], nonsaturating large magnetoresistance (LMR) [10–12], the chiral anomaly [13–16], etc. A pair of opposite monopole charges is created upon the separation of Weyl nodes under either inversion or time reversal symmetry (TRS) breaking conditions. Each of the Weyl nodes is associated with the source or sink of Berry curvature in momentum space [17,18]. While this fictitious magnetic-field-like Berry curvature couples to the external magnetic field, it gives rise to such an anomalous response in materials. Several Dirac and Weyl semimetals (DSMs and WSMs) have been proposed, and their topological signatures have been extensively investigated through photoemission and transport measurements. Another type of quasiparticle excitation, different from DSMs and WSMs, is triple point semimetal (TPSM) states [19–25]. The TPSM is believed to be an intermediate phase of relatively higher symmetric DSMs and lower symmetric WSMs. The topological index for the TPSM is still a matter of debate [26,27]; hence, it has become fertile ground for the topological study in recent times.

In the present study, we investigate the topological electronic structures of hexagonal noble-metal ruthenium, rhenium, and osmium based on symmetry analysis and *first-principles calculations* (see Sec. I of the Supplemental Material (SM) [28] for details of the computational method; see also Refs. [29–40] therein). These systems look simple at the onset, yet some of their properties are quite puzzling and still require proper understanding. One of the main motivations to choose these systems is to understand the rich physics behind the various anomalous existing experimental results such as the anomalous magnetotransport effect [41,42], the anomalous Nernst emf (and its giant quantum oscillation) [43], the measured Fermi surface (FS) [30], etc. Close inspection of these experimental results made us speculate on the topological origin of the electronic structure of these systems that could be responsible for such an anomaly. Indeed, our detailed calculations and group theoretical analysis strongly indicate the existence of multiple symmetry-protected Dirac fermionic excitations near the Fermi level E_F. We choose Ru as a case study and investigate both the bulk and surface band topologies in detail. Our calculated FS for Ru matches fairly well with the previously measured experimental FS [29].

Ru has been extensively studied for its unusual magnetotransport properties under the so-called neck-lens magnetic breakdown [41,42]. For instance, it shows nonsaturating LMR in the perpendicular magnetic field [42], which is somewhat similar to those in topological semimetals. Several theories have been proposed to address the origin of such a LMR. They are (i) linear band crossing [44–46] in momentum space as in the case of Cd_3As_2, Na_3Bi, and so on, (ii) perfect electron-hole compensation [47–50] in WSMs, WTe_2, $MoTe_2$, $PtSn_4$, and LaSb (although LaSb has trivial band ordering, multiple Weyl-type nodes are present in its band dispersion [51]), and (iii) the Lipschitz transition (LT) of the FS [50] (recently, LT was found in several topological materials where the phase

*These authors contributed equally to this work.
†aftab@iitb.ac.in
‡biswarup@iiti.ac.in

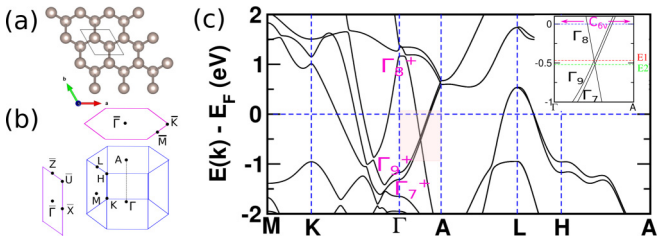

FIG. 1. (a) Top view of the $P6_3/mmc$ crystal structure of metals. (b) Brillouin zone (BZ) with high-symmetry points and their projections on the (001) and (100) surface BZ. (c) Electronic structure of Ru. The inset in (c) shows a small energy window of the shaded region along Γ-*A*. Γ_i's are the irreducible representations for the bands. The intersection of Γ_{7or8} with Γ_9 results in Dirac nodes. The red (green) dotted line is drawn to show Dirac nodes at energy E1 (E2).

transition does not break any symmetries but can be described by topological invariants). Apart from aforementioned theories, a topology-driven nontrivial origin for the nonsaturating LMR was also predicted by Tafti *et al.* [52]. Another interesting feature of Ru is that it shows a finite Nernst emf which shows giant oscillation in high-field regime [43]. The characteristic curve and the oscillation patterns are quite similar to the nontrivial material Bi_2Se_3 and very different from the Drude-like behavior [43,53]. Keeping these facts in mind, our study reveals the appearance of Dirac surface state (SS) mediated Fermi arcs on the surface of noble metals (Ru, Re, and Os), which is found to be the key origin in understanding the existing problem of transport anomalies. Note that the controversial Shockley-type SSs that appear on the surface of noble metals, such as Au, Ag, Cu, Pt, and Pd, were recently interpreted as topologically derived surface states [54].

The symmetry argument has become a very important tool to explore the material physics in recent times. The knowledge of the symmetry provides a constraint or freedom over the tunability of topological phases. We use the crystalline symmetry-breaking argument to tune the DSM phase to the TPSM phase using the alloy mechanism. For example, both Ru and Os show a Dirac nature owing to the center of inversion (IS) and C_6 rotation symmetry. However, the binary alloy RuOs breaks the IS and transforms C_6 into C_3 rotation, which converts the Dirac-like excitations to three component Fermionic excitations. The most important advantages of such symmetry-adopted tunability is that we can shift the nodal points very close to E_F depending on the crystal composition. As such, we have freedom in the position of the nodal points as well as tunability of the low-energy excitations.

II. RESULTS AND DISCUSSION

Ru, Re, and Os, in their elemental phase, crystallize in a hcp structure with the $P6_3/mmc$ space group and D_{6h} point group. The crystal structure and Brillouin zones (BZs) are shown in Figs. 1(a) and 1(b). The two-atom unit cell with particular uniaxial rotational symmetry results in a more complex electronic Fermi surface topology than the cubic noble metals (Au, Ag, Pt, etc.). The presence of the D_{6h} point group allows a little C_{6v} group along the Γ-*A* direction in the BZ. The symmetry elements that C_{6v} contains are the identity (E) operation; sixfold (C_6), threefold (C_3), and twofold (C_2) rotational symmetry about the z axis; and three vertical mirror planes σ_v and three σ_d mirror planes (σ_d bisect two σ_v mirrors). Under the spin-orbit coupling scheme, $\tilde{C}_6$ possesses six eigenvalues, namely, $e^{\pm i\frac{\pi}{6}}$, $e^{\pm i\frac{\pi}{3}}$, $e^{i\frac{\pi}{2}}$, and $e^{i\pi}$. The corresponding eigenstates for the $\tilde{C}_6$ rotation operator can be denoted as ψ_1, ψ_2, ψ_3, ψ_4, ψ_5, and ψ_6 (see Fig. S1 of the SM [28]). Now, $\tilde{\sigma}_v$ (x-axis mirror) and $\tilde{C}_6$ do not commute and thus cannot be simultaneously diagonalizable in the eigenspace of the $\tilde{C}_6$ operator. The mirror $\tilde{\sigma}_v$ keeps ψ_5 and ψ_6 invariant, i.e., $\tilde{\sigma}_v\ \psi_5 = \psi_5$ and $\tilde{\sigma}_v\ \psi_6 = \psi_6$, whereas ψ_1 will convert to ψ_2 and ψ_3 will convert to ψ_4 under the action of $\tilde{\sigma}_v$, i.e., $\tilde{\sigma}_v\ \psi_1 = \psi_2$ and $\tilde{\sigma}_v\ \psi_3 = \psi_4$. As the Γ-*A* direction is invariant under these symmetries, the noncommutating condition of $\tilde{\sigma}_v$ and $\tilde{C}_6$ enforces the formation of a doubly degenerate eigenspace by $\psi_1 + \psi_2$ (the Γ_7 representation designated by the $e^{\pm i\frac{\pi}{6}}$ eigenvalues) and $\psi_3 + \psi_4$ (Γ_8 representation designated by the $e^{\pm i\frac{\pi}{3}}$ eigenvalues) along Γ-*A*. Furthermore, ψ_5 and ψ_6 form a degenerate state (Γ_9 representation designated by the $e^{i\frac{\pi}{2}}$ and $e^{i\pi}$ eigenvalues) under the action of TRS, C_2, and σ_d symmetry. As $\tilde{C}_2$ and $\tilde{\sigma}_d$ commute, we can define a new operator, $\theta = \tilde{C}_2\tilde{\sigma}_d$. In spin rotation space, $\theta^2 = 1$. In the presence of TRS, eventually, we have $T^2\theta^2 = -1$. This is the local Kramer's theorem, which guaranteed the double degeneracy at every point along the Γ-*A* direction in the BZ as this direction is invariant under both $\tilde{C}_2$ and $\tilde{\sigma}_d$. Now, the two bands with different irreducible representations cross each other along the C_6 axis and will form gapless fourfold-degenerate Dirac nodes. For Ru, the Γ_{7or9} band intersects the Γ_8 band and forms two Dirac nodes on the C_6 rotation axis, as shown in Fig. 1(c). Similar observations and mechanisms ere also observed for Re and Os, which will be discussed later. Furthermore, in addition to the above C_{6v} symmetry element, the elements Ru, Re, and Os also have structural inversion. The interplay of inversion symmetry and TRS further ensures Kramers's double degeneracy throughout the BZ. Hence, two doubly degenerate bands belonging to different irreducible representations (IRs) while crossing each other along the C_6 direction form a Dirac node, and hence the hybridization at the nodal point is prohibited by group orthogonality relations. As such, the presence of an inversion center provides extra crystalline symmetry protection to the Dirac nodes in addition to C_{6v}. Therefore, the Dirac nodes are stable against inversion breaking perturbation in the presence of C_{6v} symmetry.

The origin of the SSs in noble metals (Au, Ag, Cu, etc.) can be traced back to Shockley's prediction [55] of SSs which appear inside an inverted energy gap due to band crossing [56,57]. Very recently, some of these Shockley SSs have been understood from the topological consideration, with the knowledge of the global properties of the electronic structure [54]. Another type of SS, called Rashba SSs, appears due to the absence of translational symmetry on the surface, which is quiet a common phenomenon on noble-metal surfaces. It should be noted that these Rashba SSs are unlike the conventional Rashba states which arise due to the breaking of inversion symmetry (in the presence of spin-orbit coupling) in bulk systems. Although these Shockley or Rashba SSs can be explained by the free-electron theory, a rigorous topological understanding is required to capture various other anomalous surface behaviors. For example, recently, Zak-phase-driven

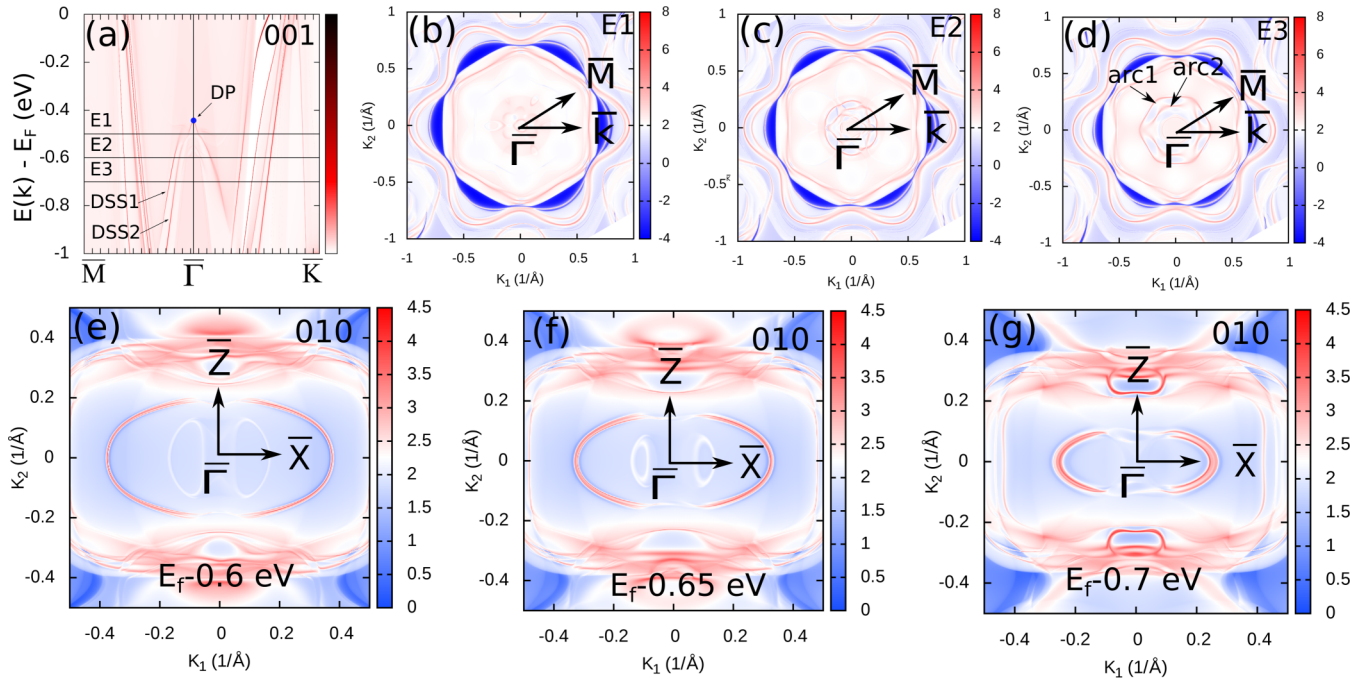

FIG. 2. (a) For ruthenium, the surface dispersion for the (001) Miller plane. (b)–(d) Fermi surface maps on the (001) surface at different energy cuts. (e)–(g) Fermi arcs at different energy cuts on the (010) side surface.

large surface polarization charge and flat SSs have been understood from the nontrivial Berry phase in topological Dirac nodal line fcc alkaline-earth metals: Ca, Sr, and Yb [58]. The topological nature of Be has also been explored, which indeed sheds light on the long-standing controversial issues of Be, such as strong deviations from the description of the nearly-free-electron theory, the anomalously large electron-phonon coupling effect [59], large Friedel oscillations, etc. [60].

In the above context, Ru, Re, and Os are unique as their Dirac-like bulk band crossing suggests the appearance of nontrivial surface dispersion and Fermi arc topology onto the surface. Since, in DSMs, the main focus is the surface states and the associated Fermi arcs that link the Dirac points, we have investigated the FS map for both the (001) and (010) surfaces for Ru, as shown in Fig. 2. Bulk projected SSs on the (001) surface are shown in Fig. 2(a). The bulk electronic structure of Ru suggests the appearance of a pair of Dirac nodes [the crossing point of the Γ_{7or9} and Γ_8 bands, as shown in Fig. 1(c) along the Γ-A direction]. The projection of these two Dirac nodes on the (001) surface falls on the $\overline{\Gamma}$ point in the surface BZ [as shown in Fig. 1(b)]. Moreover, in the energy scale, the positions of two Dirac nodes are separated by a small value. Projection of one Dirac node in the energy scale is depicted by the blue dot in Fig. 2(a). The Dirac-like surface states (DSSs) emerging from the Dirac nodes in the (001) surface are shown in Fig. 2(a). However, the other Dirac node is buried by the bulk Fermi pockets near the $\overline{\Gamma}$ point. Nonetheless, the Fermi arcs for two Dirac nodes can be clearly encapsulated a little away from the $\overline{\Gamma}$ point along the $\overline{M}$ ($\overline{K}$) direction [see Fig. 2(a)], as indicated by DSS1 and DSS2.

The FS maps on the (001) surface have been investigated, and the evolution of the FS topology is observed for three different energy cuts (E1, E2, and E3), as shown in Figs. 2(b)–2(d). At energy cut E1, the Dirac SSs, DSS1 and DSS2, are slightly immersed by bulk bands near $\overline{\Gamma}$; hence, we do not observe the clear signature of the DSS-mediated FS map at this constant energy cut. However, the signatures and contour patterns of DSS-mediated FS maps are clearly observed for other two energy cuts at E2 and E3, as described in Figs. 2(c) and 2(d). The two concentric Fermi arcs in Fig. 2(d) are indicated by arc1 and arc2. A similar pattern for the FS was previously observed by photoemission spectroscopy on the hexagonal surface of MoP [20], MoC [21], LuPtBi [61], etc. Most importantly, the FS for Ru is highly consistent with previous experiments both by angle-resolved photoemission spectroscopy (ARPES) and by de Haas–van Alphen oscillation [29,30]. However, the explanation based on the topological origin of the FS maps in those experiments is lacking.

Furthermore, the DSS-mediated Fermi arc topology can also be observed on the side surface (010 plane) of Ru. The Γ and A (L) points of the bulk BZ fall onto the $\overline{\Gamma}$ and $\overline{Z}$ points on the surface BZ (SBZ) of the (010) surface. As such, the projected Dirac nodes fall on the $\overline{\Gamma}$-$\overline{Z}$ line segment in the (010) SBZ. A time reversal pair of Dirac nodes is situated on both sides of the $\overline{\Gamma}$ point along the $\overline{\Gamma}$-$\overline{Z}$ line. In momentum space, a Fermi arc is nested between this pair of Dirac nodes, as shown in Figs. 2(e)–2(g). Figures 2(e)–2(g) show the Fermi arc topology on the side surface of Ru for three different energy cuts. For the energy cut very close to Dirac nodes [as shown in Fig. 2(e)], two arcs originating from two pairs of Dirac nodes are almost degenerate (since two nodal points are situated very close in momentum space). As we move away from the Dirac nodes, the two arcs get resolved [Figs. 2(f) and 2(g)]. We discuss and compare in detail our calculated Fermi arcs with the previously measured ARPES and transport results in Sec. III of the SM [28]. The close similarity of the calculated Fermi arc topology [in both (001) and (010) surfaces] to the measured data validate our theoretical predictions.

We now discuss the origin of these SSs and arcs from the topological perspective. A DSM phase is the parent sate of a WSM and a topological insulator (TI). The TI phase can be achieved by opening up a nontrivial gap at the nodal points. In such a case, the presence of SSs is guaranteed by the topological Z_2 index. On the other hand, two Weyl nodes with opposite Chern numbers sit together to form a Dirac node in momentum space under the precise symmetry enforcement. Such degeneracies of Weyl nodes form a "doubly degenerate" Fermi arc in the DSM phase. However, such Fermi arcs may not be protected by the topological index. Nevertheless, a crystalline-symmetry-protected three-dimensional DSM phase is stable as long as the symmetries are intact.

Further, the alloy-driven crystalline symmetry breaking allows us to realize three-component Fermionic excitation near E_F, which is different from the Dirac excitation in the pure metals Ru, OS, and Re. For the binary alloys, e.g., RuOs, the point group symmetry reduces from D_{6h} to D_{3h}. D_{3h} allows its C_{3v} subgroup symmetry along the Γ-A direction. The symmetry elements that C_{3v} contain are E, C_3, and three σ_v's (see Fig. S3 of the SM [28]). Like for the previously explained C_{6v} case, the noncommutation relation of $\tilde{C}_3$ and $\tilde{\sigma_v}$ (say, the x-axis mirror) allows two singly degenerate states (denoted by Γ_5 and Γ_6) and one doubly degenerate state (denoted by Γ_4) along the Γ-A direction in spin-orbit space. The operation of C_3 and σ_v does not alter the momentum coordinate along the k_z axis. Any accidental band crossing of Γ_{5or6} with Γ_4 along the k_z axis forms a triply degenerate nodal point (TDNP). In particular, such an alloying transforms the crystalline symmetry from C_{6v} (elemental metal) to C_{3v} (binary alloy with space group $P\bar{6}m2$), and the corresponding band representation changes as $\Gamma_{8,7} \rightarrow \Gamma_4$ and $\Gamma_9 \rightarrow \Gamma_5 \oplus \Gamma_6$. Further, the strength of the $\Gamma_{5,6}$ band splitting and the slope of the Γ_4 band collectively determine the number of TDNPs (two or four in our binary alloys) on the C_3 rotation axis. Figures 3(a) and 3(b) show a case study of the bulk band structure of the RuOs alloy. Four triple points are observed in the RuOs alloy, and they are denoted by T1, T2, T3, and T4 in Fig. 3(b). Note that TDNPs are protected by group orthogonality relations of different IRs. We have also simulated the Fermi arcs nesting on the (010) rectangular surface of the RuOs alloy, which hosts the triple point (semi)metallic state [see Fig. 3(c)]. All the TDNPs are projected along the $\bar{\Gamma}$-$\bar{Z}$ axis on both sides of the $\bar{\Gamma}$ point. The Fermi arcs originate and nest between the TDNPs, as shown in Fig. 3(c). The existence of such TDNP-induced Fermi arcs on a particular surface is a hallmark of the TPSM state for their experimental detection.

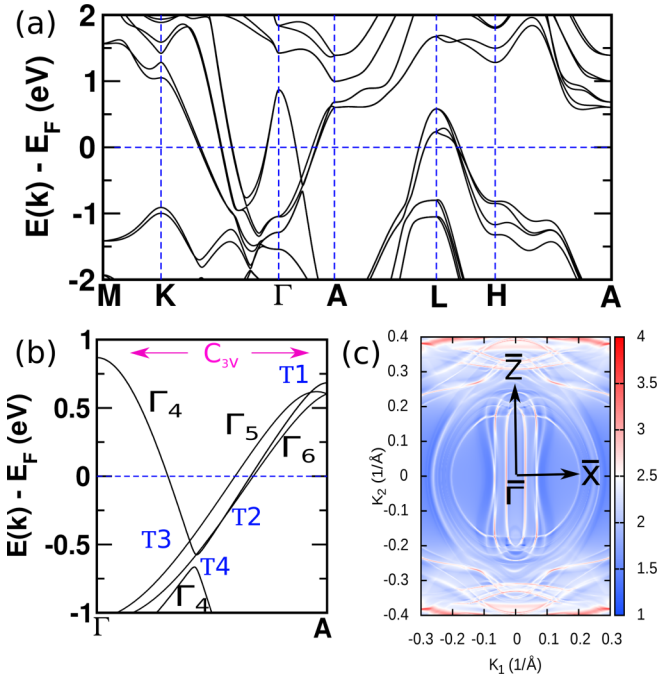

FIG. 3. For the RuOs binary alloy, the bulk band structure (a) along high-symmetry lines and (b) along Γ-A, indicating band IRs (shown by Γ_is). Triply degenerate nodal points TDNPs (shown by T's). (c) Fermi arc on the (010) side surface.

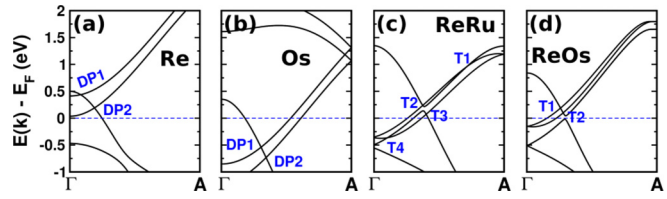

FIG. 4. Electronic structure (along Γ-A) for (a) Re, (b) Os, (c) ReRu, and (d) ReOs. Dirac points and TDNPs are represented by DP's and T's. respectively.

To get the ideal candidates [in terms of the position of Dirac points (DPs) and TDNPs with respect to E_F], we have simulated the band structures of other metals (Os and Re) and their alloys (ReRu and ReOs). The band structures along the sixfold (threefold) rotation axis are shown in Fig. 4. In Table I, we also list the compounds with the number of nodal points and their relative position in terms of energy. The spin-orbit coupling strength of Os is highest among these three pure metals; hence, the splitting between Γ_7 and Γ_9 is largest, which in turn results in a larger separation of DPs for Os in momentum space, as shown in Fig. 4(b). For the ReOs alloy, the nodal points (TDNPs) lie closer to E_F compared to the other two alloys, ReRu and RuOs. Furthermore, ReOs has only a single pair of TDNPs, as shown in Fig. 4(d).

TABLE I. Number of DPs or TDNPs and their positions $\Delta\epsilon$ with respect to E_F for pure metals and their binary alloy.

Metal	DPs	$\Delta\epsilon$ (eV)	Alloy	TPs	$\Delta\epsilon$ (eV)
Ru	2	−0.45	RuOs	4	0.60
		−0.51			−0.29
					−0.47
					−0.57
Os	2	−0.50	ReOs	2	0.17
		−0.71			0.09
Re	2	0.41	RuRe	4	0.94
		0.17			0.23
					0.06
					−0.35

TABLE II. Formation energies ΔE_{form} of the three binary alloys.

System	ΔE_{form} (meV/atom)
ReOs	−192
ReRu	−176
RuOs	−23

TABLE III. Elastic constants of binary alloys (in kbar).

System	C_{11}	C_{12}	C_{13}	C_{44}	C_{66}
ReOs	6678.8	2633.1	2185.9	2422.7	2022.9
ReRu	5617.9	2731.8	1981.2	1996.6	1443.0
RuOs	6542.1	2169.1	1949.3	2165.9	2186.5

In order to investigate the possibilities of the experimental synthesis for these binary alloys, we have checked the chemical and mechanical stability of these compounds. Chemical stability is checked by calculating the formation energies using the following formula:

$$\Delta E_{\text{form}} = E_{\text{Comp}} - \sum_{i=1}^{n} x_i E_i,$$

where E_{Comp} is the total energy of the binary alloy, E_i represents the energy of the constituent elements in their ground-state phase, and x_i is the proportion of the ith element in the binary compound. The formation energy ΔE_{form} of these three binary alloys is presented in Table II. The negative value of ΔE_{form} confirms the chemical stability of these alloys.

Apart from the chemical stability, the elastic behavior of a lattice is described by its second-order elastic constant tensor, given by

$$C_{ij} = \frac{1}{v_0}\left(\frac{\partial^2 E}{\partial \epsilon_i \partial \epsilon_j}\right),$$

where E is the total energy of the crystal, v_0 is the equilibrium volume, and ϵ denotes the strain. The stiffness tensor is symmetric and has a dimension of 6×6 for the present alloy system. For a hexagonal system, there exist five independent elastic constants. The necessary and sufficient conditions for the elastic stability of a hexagonal lattice are

$$\begin{aligned} &C_{11} > |C_{12}|, \quad 2C_{12}^2 < C_{33}(C_{11} + C_{12}), \\ &C_{44} > 0, \quad C_{66} > 0. \end{aligned} \tag{1}$$

The condition on C_{66} is redundant for hexagonal systems, with C_{11} and C_{12} given by the equation $C_{66} = (C_{11} - C_{12})/2$.

The values of the elastic constants for the three binary alloys (ReOs, ReRu, and RuOs) are listed in Table III. These values of elastic constants clearly satisfy the conditions (1) and hence confirm the mechanical stability of the three alloys.

III. CONCLUSION

The conclusion of this work is mainly threefold: (i) we predict the existence of symmetry-protected Dirac sates in the pure elemental metals Ru, Os, and Re. We find a unique Dirac-like Fermi arc topology on the (001) and (010) surfaces of these metals. Our calculated Fermi surfaces are consistent with the previous experiments by ARPES and transport measurements. (ii) The presence of such topologically nontrivial Fermi arcs can lead to a reevaluation of the understanding behind several anomalies in such metals. We speculate the topological nature of bands in Ru is responsible for several puzzling behaviors, such as magnetic breakdown, large magnetoresistance similar to that of the DSM compound Cd_3As_2, giant Nernst oscillation (similar to Bi_2Se_3), and deviations from the description of the Drude theory. (iii) By precise symmetry-breaking alloy engineering, the Dirac excitations can be tuned to three-component fermion excitations. Depending on the combinations, we get two or four pairs of TDNPs along the Γ-A directions. The position of TDNPs is very close to E_F (for the RuRe and ReOs alloys), which definitely enables the strong topological response in transport experiments. Finally, these types of transition-metal alloys are extensively synthesized and investigated in the field of catalysis; hence, our findings open up a new direction towards that too.

ACKNOWLEDGMENTS

This work was financially supported by DST SERB (Grant No. EMR/2015/002057), India. We thank IIT Indore and IIT Bombay for the laboratory and computing facilities. C.K.B. and C.M. acknowledge MHRD-India for financial support. A.A. acknowledges the National Center for Photovoltaic Research and Education (NCPRE; financially supported by the Ministry of New Renewable Energy, MNRE, government of India) for support of this research.

[1] Z. Wang, Y. Sun, X-Q. Chen, C. Franchini, G. Xu, H. Weng, X. Dai, and Z. Fang, Phys. Rev. B **85**, 195320 (2012).
[2] A. A. Soluyanov, D. Gresch, Z. Wang, Q. Wu, M. Troyer, X. Dai, and B. A. Bernevig, Nature (London) **527**, 495 (2015).
[3] A. A. Burkov, Phys. Rev. Lett. **113**, 187202 (2014).
[4] J. F. Steiner, A. V. Andreev, and D. A. Pesin, Phys. Rev. Lett. **119**, 036601 (2017).
[5] A. A. Burkov, Phys. Rev. Lett. **120**, 016603 (2018).
[6] Q. Wang, Y. Xu, R. Lou, Z. Liu, M. Li, Y. Huang, D. Shen, H. Weng, S. Wang, and H. Le, Nat. Commun. **9**, 3681 (2018).
[7] C. Shekhar, N. Kumar, V. Grinenko, S. Singh, R. Sarkar, H. Luetkens, S.-C. Wu, Y. Zhang, A. C. Komarek, E. Kampert *et al.*, Proc. Natl. Acad. Sci. USA **115**, 9140 (2018).

[8] T. Liang, J. Lin, Q. Gibson, T. Gao, M. Hirschberger, M. Liu, R. J. Cava, and N. P. Ong, Phys. Rev. Lett. **118**, 136601 (2017).

[9] F. Caglieris, C. Wuttke, S. Sykora, V. Süss, C. Shekhar, C. Felser, B. Büchner, and C. Hess, Phys. Rev. B **98**, 201107(R) (2018).

[10] Z. Li, Y. Zeng, J. Zhang, M. Zhou, and W. Wu, Phys. Rev. B **98**, 165441 (2018).

[11] Z.-M. Yu, Y. Yao, and S. A. Yang, Phys. Rev. Lett. **117**, 077202 (2016).

[12] S. Tchoumakov, M. Civelli, and M. O. Goerbig, Phys. Rev. Lett. **117**, 086402 (2016).

[13] S. Liang, J. Lin, S. Kushwaha, J. Xing, N. Ni, R. J. Cava, and N. P. Ong, Phys. Rev. X **8**, 031002 (2018).

[14] S. Jia, S.-Y. Xu, and M. Zahid Hasan, Nat. Mater. **15**, 1140 (2016).

[15] P. Kim, J. H. Ryoo, and C.-H. Park, Phys. Rev. Lett. **119**, 266401 (2017).

[16] M. Udagawa and E. J. Bergholtz, Phys. Rev. Lett. **117**, 086401 (2016).

[17] N. P. Armitage, E. J. Mele, and A. Vishwanath, Rev. Mod. Phys. **90**, 015001 (2018).

[18] X. Wan, A. M. Turner, A. Vishwanath, and S. Y. Savrasov, Phys. Rev. B **83**, 205101 (2011).

[19] Z. Zhu, G. W. Winkler, Q. Wu, J. Li, and A. A. Soluyanov, Phys. Rev. X **6**, 031003 (2016).

[20] B. Q. Lv, Z.-L. Feng, Q.-N. Xu, X. Gao, J.-Z. Ma, L. Y. Kong, P. Richard, Y.-B. Huang, V. N. Strocov, C. Fang, and H.-M. Weng, Nature (London) **546**, 627 (2017).

[21] J.-Z. Ma, J.-B. He, Y.-F. Xu, B. Q. Lv, D. Chen, W.-L. Zhu, S. Zhang, L.-Y. Kong, X. Gao, and L.-Y. Rong, Nat. Phys. **14**, 349 (2018).

[22] H. Yang, J. Yu, S. S. P. Parkin, C. Felser, C.-X. Liu, and B. Yan, Phys. Rev. Lett. **119**, 136401 (2017).

[23] C. K. Barman, C. Mondal, B. Pathak, and A. Alam, Phys. Rev. B **99**, 045144 (2019).

[24] J. Wang, X. Sui, W. Shi, J. Pan, S. Zhang, F. Liu, S.-H. Wei, Q. Yan, and B. Huang, Phys. Rev. Lett. **119**, 256402 (2017).

[25] Y. Xia and G. Li, Phys. Rev. B **96**, 241204(R) (2017).

[26] M. Kargarian, M. Randeria, and Y.-M. Lu, Proc. Natl. Acad. Sci. USA **113**, 8648 (2016).

[27] M. Kargarian, Y.-M. Lu, and M. Randeria, Phys. Rev. B **97**, 165129 (2018).

[28] See Supplemental Material at http://link.aps.org/supplemental/10.1103/PhysRevB.101.155108 for details about computations, the formation of Dirac and triple point fermion states under C_{6v} and C_{3v}, and the comparison of the simulated Fermi arcs with previous ARPES results (see also Refs. [29–40] therein).

[29] N. Nguyen, M. Mulazzi, and F. Reinert, J. Electron Spectrosc. Relat. Phenom. **191**, 27 (2013).

[30] T. Pelzer, G. Ceballos, F. Zbikowski, B. Willerding, K. Wandelt, U. Thomann, Ch. Reuß, Th. Fauster, and J. Braun, J. Phys.: Condens. Matter. **12**, 2193 (2000).

[31] P. E. Blöchl, Phys. Rev. B **50**, 17953 (1994).

[32] G. Kresse and J. Hafner, Phys. Rev. B **47**, 558(R) (1993).

[33] G. Kresse and D. Joubert, Phys. Rev. B **59**, 1758 (1999).

[34] N. Marzari and D. Vanderbilt, Phys. Rev. B **56**, 12847 (1997).

[35] I. Souza, N. Marzari, and D. Vanderbilt, Phys. Rev. B **65**, 035109 (2001).

[36] N. Marzari, A. A. Mostofi, J. R. Yates, I. Souza, and D. Vanderbilt, Rev. Mod. Phys. **84**, 1419 (2012).

[37] D. H. Lee and J. D. Joannopoulos, Phys. Rev. B **23**, 4988 (1981).

[38] D. H. Lee and J. D. Joannopoulos, Phys. Rev. B **23**, 4997 (1981).

[39] M. P. Lopez Sancho, J. M. Lopez Sancho, J. M. L. Sancho, and J. Rubio, J. Phys. F **15**, 851 (1985).

[40] Q. Wu, S. Zhang, H.-F. Song, M. Troyer, and A. A. Soluyanov, Comput. Phys. Commnun. **224**, 405 (2018).

[41] V. E. Startsev, A. N. Cherepanov, V. P. Dyakina, N. V. Volkenshteln, G. D. Kovtun, V. A. Elenskil, and V. M. Azhazha, Zh. Eksp. Theor. Fiz. **77**, 193 (1979) [Sov. Phys. JETP **50**, 98 (1979)].

[42] V. E. Startsev, V. P. Dyakina, and N. V. Volkenshtein, Pis'ma Zh. Eksp. Teor. Fiz. **23**, 43 (1976) [JETP Lett. **23**, 43 (1976)].

[43] A. N. Cherepanov, V. E. Startsev, and N. V. Volkenshtein, JETP Lett. **28**, 290 (1978).

[44] A. A. Abrikosov, Phys. Rev. B **58**, 2788 (1998).

[45] I. A. Leahy, Y.-P. Lin, P. E. Siegfried, A. C. Treglia, J. C. W. Song, R. M. Nandkishore, and M. Lee, Proc. Natl. Acad. Sci. USA **115**, 10570 (2018).

[46] J. Feng, Y. Pang, D. Wu, Z. Wang, H. Weng, J. Li, X. Dai, Z. Fang, Y. Shi, and L. Lu, Phys. Rev. B **92**, 081306(R) (2015).

[47] P. Li, Y. Wen, X. He, Q. Zhang, C. Xia, Z.-M. Yu, S. A. Yang, Z. Zhu, H. N. Alshareef, and X.-X. Zhang, Nat. Commun. **8**, 2150 (2017).

[48] M. Trescher, E. J. Bergholtz, and J. Knolle, Phys. Rev. B **98**, 125304 (2018).

[49] F. C. Chen, H. Y. Lv, X. Luo, W. J. Lu, Q. L. Pei, G. T. Lin, Y. Y. Han, X. B. Zhu, W. H. Song, and Y. P. Sun, Phys. Rev. B **94**, 235154 (2016).

[50] X. Luo, R. C. Xiao, F. C. Chen, J. Yan, Q. L. Pei, Y. Sun, W. J. Lu, P. Tong, Z. G. Sheng, X. B. Zhu, W. H. Song, and Y. P. Sun, Phys. Rev. B **97**, 205132 (2018).

[51] L.-K. Zeng, R. Lou, D.-S. Wu, Q. N. Xu, P.-J. Guo, L.-Y. Kong, Y.-G. Zhong, J.-Z. Ma, B.-B. Fu, P. Richard, P. Wang, G. T. Liu, L. Lu, Y.-B. Huang, C. Fang, S.-S. Sun, Q. Wang, L. Wang, Y.-G. Shi, H. M. Weng, H.-C. Lei, K. Liu, S.-C. Wang, T. Qian, J.-L. Luo, and H. Ding, Phys. Rev. Lett. **117**, 127204 (2016).

[52] F. F. Tafti, Q. D. Gibson, S. K. Kushwaha, N. Haldolaarachchige, and R. J. Cava, Nat. Phys. **12**, 272 (2016).

[53] B. Fauqué, N. P. Butch, P. Syers, J. Paglione, S. Wiedmann, A. Collaudin, B. Grena, U. Zeitler, and K. Behnia, Phys. Rev. B **87**, 035133 (2013).

[54] B. Yan, B. Stadtmüller, N. Haag, S. Jakobs, J. Seidel, D. Jungkenn, S. Mathias, M. Cinchetti, M. Aeschlimann, and C. Felser, Nat. Commun. **6**, 10167 (2015).

[55] W. Shockley, Phys. Rev. **56**, 317 (1939).

[56] J. Zak, Phys. Rev. B **32**, 2218 (1985).

[57] S. D. Kevan and R. H. Gaylord, Phys. Rev. B **36**, 5809 (1987).

[58] M. Hirayama, R. Okugawa, T. Miyake, and S. Murakami, Nat. Commun. **8**, 14022 (2017).

[59] R. Li, J. Li, L. Wang, J. Liu, H. Ma, H.-F. Song, D. Li, Y. Li, and X.-Q. Chen, Phys. Rev. Lett. **123**, 136802 (2019).

[60] R. Li, H. Ma, X. Cheng, S. Wang, D. Li, Z. Zhang, Y. Li, and X.-Q. Chen, Phys. Rev. Lett. **117**, 096401 (2016).

[61] Z. K. Liu, L. X. Yang, S.-C. Wu, C. Shekhar, J. Jiang, H. F. Yang, Y. Zhang, S.-K. Mo, Z. Hussain, B. Yan, C. Felser, and Y. L. Chen, Nat. Commun. **7**, 12924 (2016).